Astronomy & Astrophysics

Mathematical properties of the *SimpleX* algorithm

C. J. H. Kruip, J.-P. Paardekooper, B. J. F. Clauwens, and V. Icke

Leiden Observatory, Leiden University, Postbus 9513, 2300RA Leiden, The Netherlands
e-mail: kruip@strw.leidenuniv.nl

ABSTRACT

Context. In the *SimpleX* radiative transfer algorithm, photons are transported on an unstructured Delaunay triangulation. This approach is non-standard, requiring a thorough analysis of possible systematic effects.
Aims. We verify whether the *SimpleX* radiative transfer algorithm conforms to mathematical expectations and develop both an error analysis and improvements to earlier versions of the code.
Methods. We use numerical simulations and classical statistics to obtain quantitative descriptions of the systematics of the *SimpleX* algorithm.
Results. We present a quantitative description of the error properties of *SimpleX*, numerical validation of the method and verification of the analytical results. Furthermore we describe improvements in accuracy and speed of the method.
Conclusions. It is possible to transport particles such as photons in a physically correct manner with the *SimpleX* algorithm. This requires the use of weighting schemes or the modification of the point process underlying the transport grid. We explore and apply several possibilities.

Key words. radiative transfer – methods: analytical – methods: numerical

1. Introduction

A major challenge in computational astrophysics is to correctly account for radiative transfer in realistic macroscopic simulations. Whether one considers the formation of single stars or the evolution of merging galaxies, incorporation of radiative transfer is the next essential step of physical realism needed for a deeper understanding of the underlying mechanisms.

With the advent of the computer as an important catalyst, a myriad of efforts to solve the equations of radiative transport within a numerical framework have been developed. The resulting algorithms cover a wide range of applications where generally a method is tailored to a specific problem. In most cases, specialisation means either the choice of a specific physical scale (consider detailed models of stellar atmospheres or large-scale cosmological simulations) or emphasis on physical processes relevant to the problem at hand.

1.1. The SimpleX algorithm

The *SimpleX* algorithm for radiative transfer has been designed to be unaffected by these limitations. Owing to its modular structure, different physical processes can be included straightforwardly allowing different areas of application. More importantly, the method has no inherent reference to physical scale and thus can be applied to problems with typical length scales that lie many orders of magnitude apart. Because of its adaptive nature, many orders of magnitude in optical depth and spatial resolution can be resolved in the same simulation.

Conceived by Ritzerveld & Icke (2006) and implemented by Ritzerveld (2007), the *SimpleX* algorithm solves the general equations of particle transport by expressing them as a walk on a graph. The method can be thus considered to be a Markov Chain

on a closed graph. Transported quantities travel from node to node on the graph, where each transition has a given probability.

This approach has several advantages that we now highlight. More specifically *SimpleX*

- does not increase its computational effort or memory use with the number of sources in a simulation and consequently treats for instance scattering by dust and diffuse recombination radiation without added computational effort;
- naturally adapts its resolution to capture the relevant physical scales, (expressed in photon mean free path lengths);
- works in parallel on distributed memory machines;
- is compatible with grid-based as well as point-based hydrodynamics codes (where the latter is the more natural combination due to the point-based nature of both *SimpleX* and SPH);
- is computationally cheap because of the local nature of the Delaunay grid

1.2. Error analysis

Covering many orders of magnitude in spatial resolution (and optical depth) is a considerable challenge for radiative transfer methods in general. Approximations often need to be employed to keep the problem tractable, which makes a robust error analysis difficult.

For the vast majority of numerical methods the errors are measured by comparing with a fiducial run of the code. This is usually a simulation wherein many more time steps and/or a higher spatial resolution are used than would normally be feasible. Convergence to a solution is usually observed and this solution is accepted as the correct one, at least within the limitations of the method.

For *SimpleX* we cannot perform a similar convergence test[1]. For a spatial resolution that is significantly higher than the resolution dictated by the local mean free path length of the photons, several effects, described in Sect. 3 tend to make the radiation field more diffuse, *decreasing* instead of *increasing* accuracy. This property of *SimpleX* is not a weakness but instead inherent to the method using a *physical* grid wherein deviations from its natural resolution often cause a deterioration in the solution.

Because of its mathematically transparent nature, the *SimpleX* algorithm has the great advantage that one can assess its error properties analytically. The resulting prescriptions are quite general and can be applied to different regions of parameter space, an advantage over the "numerical converge approach" usually applied in the error analysis of radiative transfer methods. The development of analytical descriptions and the discussion of their implications will be the main focus of this text.

1.3. Outline

Given the desirable properties of the *SimpleX* algorithm, we aim to assess whether the inaccuracies that inevitably arise in a numerical method can counterweigh *SimpleX*'s virtues.

We will demonstrate that the use of high dynamic range Delaunay triangulations as the basis of radiative transfer introduces systematic errors that manifest themselves as four distinct effects: diffusive drift, diffusive clustering, ballistic deflection, and ballistic decollimation. We describe and quantify these effects and, subsequently, provide suitable solutions and strategies. We than demonstrate how the derived measures can be used to constrain the translation of a physical problem to a transport graph in such a way as to avoid or minimise errors. We finally discuss our results in a broader picture and outline related and future work, specifically an implementation of a dynamically updating grid in *SimpleX*.

Although developed in the context of *SimpleX*, many of our results are relevant for other transport algorithms that work on non-uniform grids (AMR grids or SPH particle sets).

2. Radiative transfer on unstructured grids

We describe the three means of transport that constitute the *SimpleX* algorithm. Starting from a general description of the equation of radiative transfer in inhomogeneous media, we delve into the specifics of *SimpleX*. This requires us to introduce the Delaunay triangulation, which lies at the heart of our method and plays a central role in this text.

2.1. General radiation transfer

The equation of radiative transfer for a medium whose properties can change both in space and time is given by

$$\frac{1}{c}\frac{\partial I_\nu}{\partial t} + \hat{n} \cdot \nabla I_\nu = \eta_\nu - \chi_\nu I_\nu, \tag{1}$$

where $I_\nu \equiv I(t, x, \Omega, \nu)$ is the monochromatic specific intensity, $\hat{n}$ is a unit vector along the ray, and η_ν and χ_ν are the monochromatic emission and opacity coefficients, respectively.

If $\frac{1}{c}\frac{\partial I_\nu}{\partial t} \ll 1$, in other words, if I_ν is not explicitly time dependent *or* the time and space discretisation is such that c can be considered infinite, this equation simplifies to

$$\hat{n} \cdot \nabla I_\nu = \eta_\nu - \chi_\nu I_\nu. \tag{2}$$

If we take the spatial derivative along the ray and divide by χ_ν, Eq. (2) can be rewritten as

$$\frac{\partial I_\nu}{\partial \tau} = S_\nu - I_\nu, \tag{3}$$

where we define the source function $S_\nu \equiv \eta_\nu/\chi_\nu$ and optical depth $d\tau \equiv \chi_\nu ds$ and s parametrises the distance along the ray. Equation (3) can be solved numerically if η_ν and χ_ν are known locally, the meaning of "local" depending on the type of discretisation of the volume. The form of Eq. (3) suggests that the optical depth is the most natural variable to discretise. In general, this will produce cells of unequal volume and, hence, an irregular computational mesh. As mentioned in Sect. 1 and explained in more detail in Sect. 6, we generate a set of nuclei that reflects the underying optical depth field and connect these nuclei with a Delaunay triangulation.

2.2. A natural scale

The fundamental idea behind the *SimpleX* algorithm is that there exist a natural scale for the description of radiative processes: the photon local *mean free path*

$$l_{\text{mfp}} \equiv \frac{1}{\sigma n}, \tag{4}$$

where σ is the total cross-section and n the number density of the particles responsible for the extinction. Since photons travel typically one mean free path before interacting with the medium, information on a much smaller scale does not necessarily yield a deeper understanding of the physical problem at hand.

Following this line of reasoning, the next step is to choose a computational mesh that inherently carries this natural scale, in other words, use an irregular grid whose resolution adapts locally to the mean free path of the photons traveling over it[2].

2.3. The grid

This computational mesh or transport graph is constructed by first defining a point process that represents the underlying (physical) problem and second by connecting these points according to a suitable prescription.

The point process is defined by prescribing the local point field density as a function of the scattering and absorption properties of the medium through which the particles propagate. The resulting points are connected by means of the unique *Delaunay triangulation* (Delone 1934). Thus, the points that carry the triangulation, which we refer to as *nuclei* in the remaining text, are connected as a graph, along whose connecting lines (called *edges*) the particles are required to travel.

This decision to construct a transport graph has several advantages: first, the connection with the physical processes is evident; second, the Delaunay triangulation (and the dual graph, the *Voronoi tessellation* (Voronoi 1908)) is unique and is in many respects the optimal unstructured partitioning of space

---

[1] This is possible, however, if the direction-conserving transport to be introduced in Sect. 2.5.3 is used. Alternatively, several instances of the same simulation with a different random seed for the grid construction can be averaged to obtain error estimates as well.

[2] In our implementation, we use a single frequency bin and an effective cross-section such that the mean free path depends on the number density and the point-to-point distance only.

(Schaap & Van de Weygaert 2000); third, the Voronoi-Delaunay structures carry all information required for the transport process, making the transport step itself very efficient.

We note that the use of Voronoi-Delaunay grids does not imply that the transfer of photons has to proceed along the edges of the Delaunay triangulation. Another approach would be to trace rays through either the Voronoi cells or Delaunay simplices. This ray-tracing could be done classically with long characteristics (Mihalas & Weibel Mihalas 1984) or using Monte Carlo methods (Abbott & Lucy 1985). In SimpleX, the photons travel from cell to cell interacting with the medium as they proceed. In this sense, the transport of radiation is treated as a local phenomenon and the global nature of the radiative transfer problem is dealt with by sufficient iterations of this local transport. The intimate relation between the structure of the grid and the transport of the photons is one of the reasons why the *SimpleX* algorithm is exceptionally efficient.

The construction of the grid itself is a task performed by dedicated software freely available on the web. Once the generating nuclei have been given, the Voronoi-Delaunay structure is unique. In creating the distribution of generating nuclei, we can manipulate the properties of our computational grid. The translation from a given density (opacity) field as either particles or cells to a Voronoi-Delaynay grid optimal for *SimpleX* is a fundamental part of the algorithm.

2.4. Voronoi-Delaunay structures

Because it plays a central role in this text, we now proceed with a concise introduction to the Voronoi-Delaunay grid.

We introduce a set of nuclei in a *D*-dimensional space together with a distance measure (in all of our applications, we use the isotropic "Pythagoras" measure). We partition this space by assigning every one of its points to its nearest nucleus. All the points in space assigned to a particular nucleus *n* form the *Voronoi region* of nucleus *n* (if $D = 2$, the region is often called the *Voronoi tile*). By definition, the Voronoi region of *n* consists of all points of the given space that are at least as close to *n* (according to the distance measure of that space) as to any of the other nuclei. The set of all points that have more than one nearest nucleus constitute the *Voronoi diagram* of the set of nuclei (Edelsbrunner 2006; Okabe et al. 2000; O'Rourke 2001; Vedel Jensen 1998). For clarity, most of our explanatory illustrations will use $D = 2$ (see Fig. 1 for an example in the plane), but our applications have $D = 3$.

The set of all points that have exactly two nearest nuclei n_1, n_2 is the *Voronoi wall* between these nuclei. If $D = 2$, this wall is a line; if $D = 3$, it is a plane; and so on. In our astrophysical applications, $D = 3$, in which case (pathological configurations excepted) triples of planar walls come together in *lines*, the points of which have three nearest nuclei; the lines, finally, join in quadruples at *nodes*, single points that have four nearest nuclei. A Voronoi wall thus separates the Voronoi regions around two nuclei. The connection between these nuclei, called an *edge*, is the geometric dual of the wall. The set of all edges is the *Delaunay triangulation* (Delone 1934) of the point set. The Delaunay triangulation can be defined as the unique triangulation of nuclei for which the interior of a Delaunay simplex (triangle in two dimensions) contains no other nuclei.

In our algorithm, no other connections between nuclei are allowed, hence only adjacent Voronoi regions are connected. The expectation value for the number of these *Delaunay neighbours*, Λ, is 6 in 2D and 15.54⋯ in 3D. Voronoi regions based on an isotropic distance measure are convex; for a point process
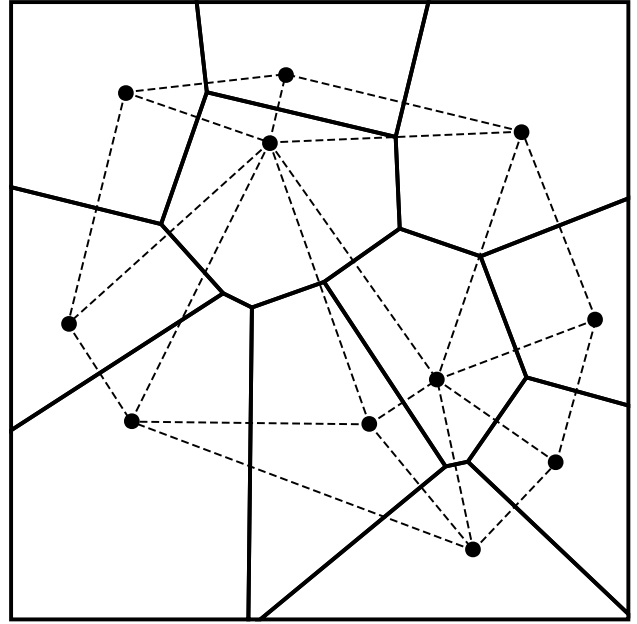

Fig. 1. Voronoi tessellation of the plane (solid lines). Each cell contains all points that are closer to its nucleus (indicated by a dot) than to any other nucleus. The corresponding Delaunay triangulation is shown in dashed lines. Note: only visible nuclei are included in the triangulation.

containing *N* nuclei, the number of geometric entities (walls, edges, nodes, etc.) is $O(N)$.

For our application to transport theory, it is most important that the Delaunay triangulation has a minimax property, i.e. it is the triangulation with the largest smallest angle between adjacent triangle edges. Of all possible triangulations of a given point set, the Delaunay triangulation is the one that maximises the expectation value of the smallest angle of its triangles. In more colloquial terms, the Delaunay triangulation has the least "sliver-like" triangles, and the most "fat" triangles.

Another advantageous property of the Delaunay triangulation is that every edge pierces the wall between the Voronoi regions that it connects at right angles. This justifies the use of Eq. (3) where the spatial derivative is taken along the ray.

2.5. Three types of transport

In SimpleX, transport is always between neighbouring Voronoi cells i.e., those connected by the Delaunay triangulation. On average, every nucleus has 6 neighbours in 2D and 15.54⋯ neighbours in 3D. When photons travel through a cell, the optical path length, *l*, is taken to be the average length of the Delaunay edges of that cell. If the number density of atoms in the cell is given by *n* the fraction of photons that are removed from the bundle, $N_{\rm rem}$, is given by

$$N_{\rm rem} = N_{\rm in} e^{-n\sigma l}, \tag{5}$$

where σ is the total cross-section that may be due to multiple extinction processes.

In general, extinction can be subdivided into absorption and scattering. Radiation that is removed by absorption processes will in general change the both the temperature of the medium and its chemical state but need not be transported further at this point.

Photons that are removed from the bundle by scattering should propagate to neighbouring cells, either isotropically or
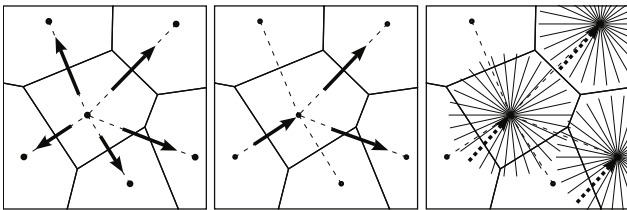
Fig. 2. Three principal means of transport supported in *SimpleX*. *Left panel*: diffuse transport, photons from the incoming edge (not shown) are distributed outward along all edges (including the incoming edge). *Central panel*: ballistic transport, photons are transported along the D edges directed most forward with respect to the incoming direction. *Right panel*: direction-conserving transport, photons (indicated with the dotted arrows) are transported as in ballistic transport but their direction is stored indefinitely in a global set of solid angles.

with a certain directionality[3]. This can be accomplished using the *diffuse transport* method schematically depicted in the left panel of Fig. 2 and explained in more detail in Sect. 2.5.1. The radiation that is not removed from the bundle, however, needs to travel straight on along the original incoming direction. For optically thick ($\Delta\tau > 1$) cells, we simulate this using *ballistic transport* (see the central panel of Fig. 2 and Sect. 2.5.2).

In regions of the grid where the cells are optically thin ($\Delta\tau < 1$), ballistic transport becomes too diffusive and we need to resort to *direction-conserving transport* or DCT (see the right panel of Fig. 2 and Sect. 2.5.3).

We now proceed by describing these transport methods in more detail and show how they are combined in a general simulation.

2.5.1. Diffuse transport

We begin with the description of conceptually the simplest form of transport implemented in *SimpleX*. At each computational cycle, which we refer to as *sweep*[4] in the remaining text, the content of each nucleus is distributed equally among its neighbouring nuclei (see the left panel of Fig. 2.) We call this kind of transport *diffuse* because it has no memory of direction. For a homogeneous distribution of nuclei, the transported quantity will diffuse outwards, spreading spherically from the position of a source. This type of transport is appropriate for photons that are either scattered diffusely or absorbed and re-emitted in random directions.

2.5.2. Ballistic transport

We now consider a group of photons that is transported along a Delaunay edge to a certain nucleus. We assume that the nucleus represents a finite optical depth. A fraction of the photons will be removed from the group by the interaction and another fraction will fly straight onward. Diffusive transport is not suited to describing this behaviour, so we introduce *ballistic* transport.

In the ballistic case, the incoming direction of the photons is used to decide the outgoing direction (introducing a memory of one step into the past). In the generic Delaunay triangulation, there is no outgoing edge parallel to the incoming one, so the

---

[3] As we see in Sect. 4.1, anisotropic scattering processes can be simulated straightforwardly by assigning weights to the outgoing edges so that more radiation is transported in the appropriate directions.

[4] Although in our current implementation each photon takes exactly one step per sweep, this need not in general be the case.
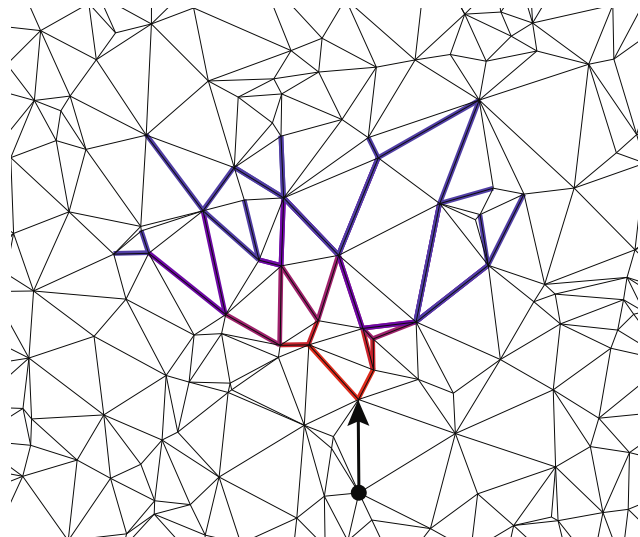
Fig. 3. Example of decollimation in the plane for five ballistic steps. The arrow indicates the initial influx of photons. According to the ballistic transport mechanism, photons are transported along the D most forward edges with respect to the incoming direction. The colour coding is as follows: with every step the photons acquire a colour that is less red and more blue. As the angle between adjacent edges is large in 2D (60 degrees on average), the bundle loses track of its original direction in only a few ballistic steps.

outgoing photons are distributed over the *D* most forward pointing edges, where *D* is the dimension of the propagation space (see centre panel of Fig. 2.) As such, we ascertain that for an isotropically radiating source the complete "sky" is filled with radiation because the opening angle associated with each edge on average corresponds to $2\pi/\Lambda$ or $4\pi/\Lambda$ in two and three dimensions respectively[5].

Because of the random nature of the directions in the Delaunay grid, we note that radiation will tend to lose track of its original direction after several steps, a property that we call *decollimation* as it will steadily increase the opening angle of a beam of radiation as it travels along the grid (see Fig. 3). This property renders ballistic transport appropriate for highly to moderately optically thick cells only, where just a negligible amount of radiation has to be transported more than a few steps. If we take unity as a lower limit to the optical depth of a cell for which ballistic transport is used, at every intersection a fraction of $(1 - 1/e)$ of the photons becomes absorbed and the cumulative average deflection (decollimation) θ becomes

$$\theta = \theta_{\mathrm{D}} \sqrt{\sum_{n=1}^{\infty} \frac{1}{e^n}} = \theta_{\mathrm{D}} \sqrt{\frac{1}{e-1}} \approx 0.76\,\theta_{\mathrm{D}}, \tag{6}$$

where θ_{D} is the decollimation angle per ballistic step. In Sect. 3.3.1, we measure θ_{D} and describe the consequences of decollimation in more detail.

A visual extension of the statement given by Eq. (6) is shown in Fig. 4. From the figure, it is evident that the fraction of photons that is (ever) deflected more than 45° centred around the initial direction falls off sharply with the optical depth of a cell. Only for optically thin (say 0.2) cells, the fraction of photons whose deflection stay under 45° is lower than 0.5.

---

[5] Another way to look at this is that, for an isotropically emitting source, the number of nuclei that receive radiation must scale as the square (cube) of the travelled distance for two (three) dimensions.
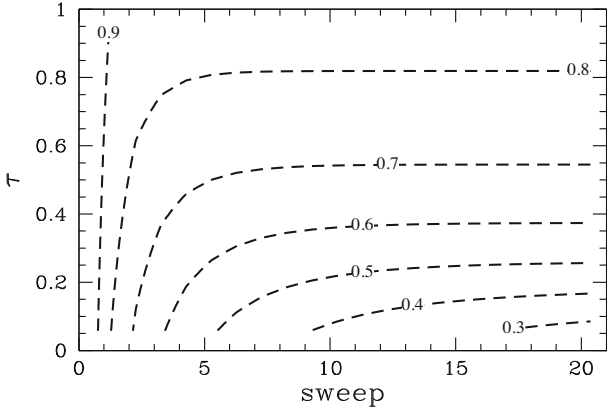
Fig. 4. Fractions of photons (contours) with deflection angle within 45° of the initial direction as a function of the number of ballistic steps (abscissa) and optical depth (ordinate). From the figure, it is evident that decollimation of photons is only potentially problematic when the cells are very optically thin.

In realistic cosmological simulations, the effect of decollimation results in diffusion that softens shadows behind opaque objects (e.g., filaments and halos). The diffuse radiation field will penetrate into the opaque objects and ionise the high density gas inside. This results in ionisation of dense structures at too early times and the stalling of the ionisation front farther from the source. This clearly necessitates the introduction of a means of transporting photons in the optically thin regime.

2.5.3. Direction-conserving transport

If the cells are optically thin, the loss of directionality introduced by ballistic transport over many steps becomes prohibitively great and we switch to *direction-conserving* transport (DCT for short). Here the radiation is confined in solid angles corresponding to global directions in space: if a photon has been emitted in a certain direction associated with a solid angle, it will remember this direction while travelling along the grid. This effectively decouples the directionality of the radiation field from the directions present in the grid (see right panel of Fig. 2.)

For an example of the improvement of DCT over ballistic transport in a realistic case see Fig. 5. The contour for DCT shows a sharp "shadow" (in good agreement with the C²-ray result) where the dense filament is left neutral whereas ballistic transport results in a more diffuse, softer, shadow. Moreover, the ballistic ionisation front stalls with respect to the DCT result. This is another symptom of spurious diffusion: the positive radial component of the diffuse radiation is smaller than it should be resulting in more ionisations close to the source and less flux into the ionisation front.

We note, however, that the transport of photons still occurs along the three most forward directed Delaunay edges of the grid, where "forward" is now with respect to the global directions of the solid angles[6]. These edges may lead to nuclei that lie outside the solid angle associated with the direction of the photons.

In this sense, we now have two types of angular resolution in our method. The first is related to the size of the solid angle in which radiation is confined spatially, which is set by the number of Voronoi neighbours of a typical nucleus ($15.54\cdots$ in 3D). We

---

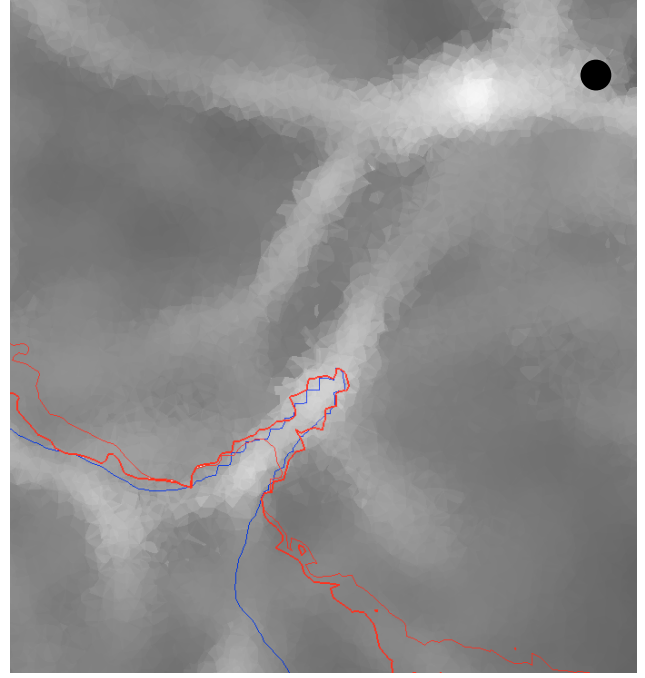[6] DCT can thus be viewed as ballistic transport with complete memory of direction.

Fig. 5. Shadow behind a dense filament irradiated by ionising radiation (indicated as a black dot). The hydrogen number density is plotted logarithmically in greyscale and ranges between 2.8×10^{-5} to 0.12 cm^{-3}. The red and blue lines indicates the contour where the neutral fraction of hydrogen is 0.3. The thin and thick red lines are for ballistic and direction-conserving transport (DCT) respectively. The blue line is obtained with the C²-ray code (Mellema et al. 2006).

call this *spatial resolution* and emphasize that it depends solely on the nature of the Delaunay triangulation and as such is not adjustable. The second type of angular resolution is set by the global division of the sky into arbitrarily many directions (not necessarily constant along the grid) and we call this the *directional resolution*. For the tests presented here, we use 40 directions (a directional resolution of 40), implying a solid angle of $\pi/10$ sr for each unit vector.

A technical consequence of the approach sketched above is the need to divide space into equal portions of solid angle whose normal vectors are isotropic. There are many ways to divide the unit sphere into equal patches but the requirement of isotropy in general cannot be met exactly.

For maximal flexibility in angular resolution, we construct sets of unit vectors that are distributed isotropically in angle using a simulated annealing scheme.

One major drawback of the introduction of global directions in the simulation is that they will give rise to artifacts much like those observed in hydrodynamical simulations on regular grids. This must in turn be counteracted by the randomisation of these global directions at appropriate time intervals, which makes DCT computationally relatively expensive.

2.6. Combined transport

The three means of transport described above in general are applied simultaneously. If the total optical depth τ_{tot} for a given cell is caused by multiple extinction processes

$$\tau_{tot} = \sum_i \tau_i, \tag{7}$$

the fraction, f_i, of the incoming ray of photons that will be removed by process i is given by

$$f_i \equiv \frac{\tau_i}{\tau_{\text{tot}}} \, . \tag{8}$$

Depending on the physical nature of this process, the photons are either removed from the bundle (to heat up the medium) or redistributed isotropically (or with some directionality) using diffuse transport. The remaining photons (those that are not removed from the ray) are transported with either ballistic or direction-conserving transport, depending on the total optical depth of the cell (ballistic if $\tau_{\text{tot}} \geq 1$ and DCT if $\tau_{\text{tot}} < 1$). The fraction of the incoming photons that is treated with one of the three transport methods is thus fully determined by the grid.

3. Anisotropy and its consequences

Notwithstanding the "ideal" properties of the Delaunay triangulation, the probability density distribution of the angle between adjacent Delaunay edges is quite broad (Icke & van de Weygaert 1987; Okabe et al. 2000, Sect.5.5.4), so that, even though the average triangle is the "fattest" possible, many "thin" triangles will occur. This situation may be changed by iteratively adapting the underlying point process, in such a way that each nucleus comes to coincide with the centre-of-mass of its Voronoi region (see Lloyd 1982, for such an algorithm), resulting in so-called Centroidal Voronoi Tessellations (see e.g. Du et al. 1999). This procedure produces "most spherical" Voronoi regions (hexagons if $D = 2$), but is in general far too costly for practical computations in which the triangulation must be re-computed frequently. Moreover, the shifting of the nuclei implies that the connection with the physical properties of the underlying medium is no longer entirely faithful. Another reason to refrain from the use of Centroidal Voronoi Tessellations is the introduction of regularity and hence symmetry in the grid. In two dimensions, for instance, the hexagonal Voronoi cells tend to align, introducing globally preferential directions in the transport of radiation. This will inevitably give rise to artifacts in the radiation field transported on such a grid.

Although the Voronoi-Delaunay construction is the optimal choice for the tessellation of a random (Poisson process) point set, it is not obvious that this is true when the point set is inhomogeneous or anisotropic. Inhomogeneity is, of course, the property we encounter in all practical cases. The probability distribution of the directions of Delaunay edges on a Poisson nucleus is isotropic, but this is no longer the case when the distribution of the nuclei is structured.

This inherent anisotropy of the graph introduces a bias that is the cause of some undesirable effects. It is these effects, and their treatment, that we consider here. We have tried in vain to find a mathematical treatment of related questions, such as: (1) is the Delaunay triangulation the one that maximises the isotropy of the edges emanating from a given nucleus? (2) can a process be found that adjusts the positions of the nuclei in such a way as to increase the isotropy of the edges? Concerning (1), we conjecture that the answer is yes, because (at least superficially) that would seem to follow from the minimax property of the angles between the edges. As to (2), we have looked for a procedure analogous to the "centre-of-mass" stratagem mentioned above, but have been unable to find one.

Thus, we must face the consequences of the anisotropy bias on inhomogeneous point processes. We note in passing that this bias will exist locally even in the case of a Poisson process for placing the nuclei, because, due to shot noise, every instance of

a random point process is locally anisotropic, even if homogeneous and isotropic when averaged over multiple instances.

3.1. Error measure

For a homogeneous Poisson distribution of nuclei, the expectation value for the number of Delaunay neighbours (and thus edges), Λ, is 6 in two- and $15.54\cdots$ in three-dimensional space. These Delaunay edges have no preferential orientation and their statistical properties are well known (e.g. Okabe et al. 2000).

We now consider an inhomogeneous distribution of nuclei. Spatial gradients then appear in the density of nuclei, $n(\boldsymbol{x})$, and the Delaunay edges connecting these nuclei are no longer distributed evenly over all possible orientations. For a given nucleus, there will be, on average, more edges pointing towards high-density regions than away from them.

This can be quantified as follows. Without loss of generality, we may assume a number density of nuclei that has a gradient in some fixed direction x provided that the characteristic length scale of the gradient is much larger than the mean distance between nuclei, a provision we assume to be fulfilled from now on.

We take a cross-section perpendicular to the direction of the gradient through the box at an arbitrary position x_0. The resulting plane of surface S is pierced by Delaunay edges connecting nuclei on either side of the plane.

The number of edges piercing the plane can be estimated as follows. The local density of edges is the product of the number density of nuclei and Λ. An edge is able to pierce the plane when two requirements concerning its orientation are fulfilled:

1. its projected length must be larger than the distance between its originating nucleus and the plane.
2. it must point in the correct direction.

The expectation value of the Delaunay edge length, $\mathcal{D}$, is given by

$$\mathcal{D} = \xi n(x)^{-1/3}, \tag{9}$$

in three dimensions, where $\xi = 1.237\cdots$ (Ritzerveld 2007, Eq. (3.22)). An edge emanating from a nucleus at position x will thus only pierce the plane if its projected length exceeds $\Delta x \equiv |x - x_0|$. Hence, the first requirement is fulfilled when

$$\Delta x \leq \mathcal{D} \cos\theta, \tag{10}$$

where θ is the angle between the edge and the direction of the gradient. The orientation of these edges is random[7], so we must average the cosine over a half sphere, which yields a factor of one half. The effective length of the edges is thus $\mathcal{D}/2$, which implies that only nuclei inside a slab of thickness $\mathcal{D}$, centred at x_0 contribute to the density of piercing edges.

The second requirement effectively excludes half (up to first order) of the edges because they point away from the plane. This statement is equivalent to noting that every piercing edge connects exactly two nuclei at opposite sides of the plane. By including both factors, we find that the number of piercing lines, N_{p}, is given by

$$N_{\text{p}}(x) = \frac{n(x)\Lambda\mathcal{D}S}{4} \, . \tag{11}$$

---

[7] The orientation might be correlated with the direction of the gradient but we neglect this at the moment because it would only influence our results to second order.

The surface density of lines piercing the slab, $\sigma(x)$, is now simply defined by

$$\sigma(x) = \frac{N_p}{S} = \frac{n(x)\Lambda\mathcal{D}}{4} . \qquad (12)$$

The sought-after fractional excess, $E(x)$, of parallel (with respect to the gradient) over anti-parallel Delaunay edges is thus given by differencing $\sigma(x)$ over a sufficiently small[8] interval Δx and division by $\Lambda n(x)$

$$E(x) \equiv \frac{1}{\Lambda n(x)} \frac{\Delta\sigma(x)}{\Delta x} = \frac{\xi}{4n(x)^{4/3}} \frac{\Delta n(x)}{\Delta x}, \qquad (13)$$

where we used Eq. (9) to eliminate $\mathcal{D}$. The excess of edges pointing towards higher density region may have a signifcant effect on quantities transported along these edges. In the next three sections, we describe and quantify these effects. We note in passing that in many practical applications (see also Sect. 6) the point density $n(x)$ of nuclei is taken to be proportional to a power α of the mass density $\rho(x)$

$$n(x) \propto \rho(x)^{\alpha}. \qquad (14)$$

In that case, Eq. (13) becomes

$$E(x) = \frac{\xi}{4n(x)^{1/3}} \frac{\Delta\log n(x)}{\Delta x} = \frac{\alpha\mathcal{D}}{4} \frac{\Delta\log\rho(x)}{\Delta x} . \qquad (15)$$

If $\alpha = 3$, the length $\mathcal{D}$ is proportional to the mean free path of the photons (Ritzerveld & Icke 2006). In many respects, this is the "ideal" case, because it is in fact "transport-homogeneous" as experienced by the photon, every step being of equal optical depth. However, Eq. (15) shows that this "ideal" case has a gradient asymmetry that is three times worse than is the case if $n(x) \propto \rho(x)$.

3.2. Effects on diffusive transport

In Sect. 2.5.1, we stated that for diffusive transport in a homogeneous distribution of nuclei, the radiation propagates spherically away from a source. On a graph corresponding to an inhomogeneous distribution of nuclei, however, this is not the case. The spreading of the transported quantity will no longer be spherical anymore for two reasons:

1. the Delaunay edges are shorter when the nuclei are spaced more closely.
2. the orientation of the Delaunay edges is no longer isotropic: more edges point towards the overdense regions.

3.2.1. Physical slow down

The first reason reduces the transport velocity and can be interpreted as a physical phenomenon. If we were to identify the length of a Delaunay edge with the local mean free path of the transported quantity (e.g. photons), the shorter edges would simply express that we have entered a region of increased optical depth where it takes a greater number of mean free path lengths to traverse a given physical distance. It has been shown (Ritzerveld & Icke 2006) that identifying the average Delaunay edge length with the local mean free path of the relevant processes is natural choice when constructing the triangulation and the observed behaviour is therefore both expected and physical.

---

[8] We emphasize the discrete nature of this derivative by noting that $\Delta n = \frac{dn}{dx}\Delta x = \mathcal{D}\frac{dn}{dx} = \xi n(x)^{-1/3}\frac{dn}{dx}$ etc.
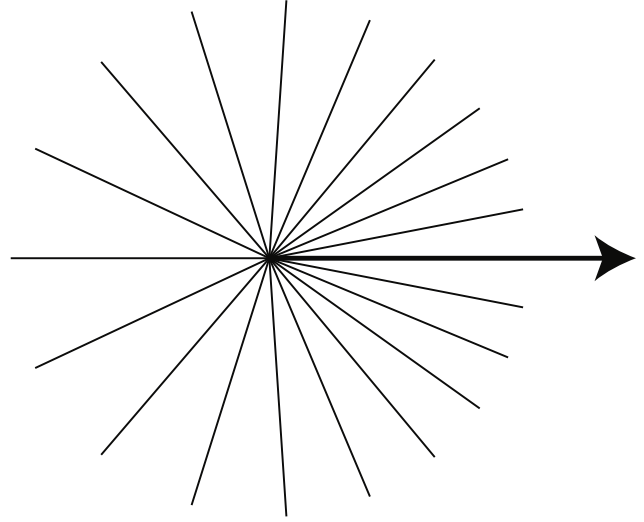

Fig. 6. Schematic example of a nucleus and its edges subject to a gradient in the number density of nuclei in the positive x-direction. More edges point toward the overdense region (along the gradient). If every edge were to transport an equal number of photons to neighbouring nuclei, the anisotropy of outgoing edges would produce an unphysical net flow along the gradient indicated by the arrow, which is the vector sum of the edges scaled down by roughly a factor of three.

3.2.2. Drift

The second reason, quantified by Eq. (13), is an artifact of the Delaunay triangulation itself and causes unphysical behaviour. When too many edges are pointing into the overdense regions, the transported particles are deflected into those regions and the direction of propagation tends to align with the gradient (see Fig. 6 for an example in the plane). We call this effect *drift* and now proceed to quantify its consequences for diffusive transport.

A photon scattering at a nucleus has the following probabilities of moving in the dense (subscript d) or underdense (subscript u) direction:

$$\begin{aligned} p_d &= \frac{1}{2} + \frac{E(\boldsymbol{x})}{2} \\ p_u &= \frac{1}{2} - \frac{E(\boldsymbol{x})}{2}. \end{aligned} \qquad (16)$$

The expectation value d_D of the drift per scattering event is therefore proportional to the $E(\boldsymbol{x})$ part of an outgoing edge in the direction of the dense region. The multiplication factor, which can be found by integrating over a half-sphere, is $1/2$ since not all edges point exactly to the right giving

$$d_D = \frac{\mathcal{D}}{2} E(\boldsymbol{x}), \qquad (17)$$

in which $\mathcal{D}$ is again the expectation value of the Delaunay edge length (see Eq. (9)).

We consider a scattering experiment where a number of photons is placed at one position of a triangulation with a density gradient. We expect the photons to diffuse outward with an ever decreasing radial velocity (the distance travelled, L, scales with the root of the number of steps) and at the same time drift towards the dense region with a constant velocity. There comes a time (or distance) at which the drift is equal in magnitude to the diffusion radius. We define the drift length, L_{drift}, as the scale on which the diffusion distance is equal to the distance travelled through drift. Roughly speaking, diffusion dominates for

$L < L_{\text{drift}}$ and drift dominates for $L > L_{\text{drift}}$. Setting the diffusion distance equal to the distance travelled through drift,

$$\mathcal{D}\sqrt{N_E} = \frac{\mathcal{D}}{2}E(\boldsymbol{x})\,N_E, \tag{18}$$

we find that the number of steps at equality is given by

$$N_E = 4/E^2(\boldsymbol{x}). \tag{19}$$

Using Eq. (9) and (13) gives an equality length of

$$L_{\text{drift}}(\boldsymbol{x}) = \frac{8n(\boldsymbol{x})}{|\nabla n(\boldsymbol{x})|}, \tag{20}$$

independent of $\mathcal{D}$. Hence we have found a *local* expression for the relative importance of the unphysical drift.

For a given density distribution $n(x)$, the length $L_{\text{drift}}(\boldsymbol{x})$ can be evaluated everywhere[9]. This parameter can be interpreted as follows. We define the minimum $L_{\text{drift}}(\boldsymbol{x})$ for all $\boldsymbol{x}$ to be N times the box side length, such that the drift can be at most $1/N$ of a box side while the radiation scatters throughout the box. In any case, we must ensure that $L_{\text{drift}}(\boldsymbol{x})$ is much longer than the box side length.

Thus, even if the density contrast is very small, it must not fluctuate too severely. We note that it does not help to increase the number of nuclei, since both $n(\boldsymbol{x})$ and $\nabla n(\boldsymbol{x})$ in Eq. (20) scale with that number. Using more nuclei reduces the anisotropy per nucleus, Eq. (13), but because the number of steps to be taken increases accordingly, the effect simply adds up to the same macroscopic behaviour. Only the shape of $n(\boldsymbol{x})$ determines the magnitude of $L_{\text{drift}}(\boldsymbol{x})$.

To determine the resulting constraint on the grid, we consider the case in which $L_{\text{drift}}(\boldsymbol{x})$ does not depend on position. Setting $L_{\text{drift}}(\boldsymbol{x}) = $ constant in Eq. (20) defines an exponential density distribution, where the anisotropy is smeared out maximally over the domain. In this case, if we wish the drift to be less than $1/8$ of the box length, the density contrast must be less than a factor $e \approx 2.71 \cdots$ implying that the restrictions put by our isotropy demands are rather stringent.

3.2.3. Clustering

We have seen that the spurious drift for diffuse scattering places restrictions on the density contrasts that can be simulated by the plain implementation of *SimpleX* introduced in Sect. 3.2.2. We have assumed that the scale of the density fluctuations is comparable to the box size. This is not a restriction: if we are interested in a case where the density fluctuations are of a much smaller scale than the box size, we can just place an imaginary box around each density fluctuation and use all the quantitative results from above. In doing so, we see that for any given "snapshot" too many photons will be present in the local overdense regions, but if there are no overall density contrasts on large scales, there will be no significant macroscopic drift. The effect of the local drift on small scales can, however, still influence results on a large scale. Not only does the drift influence the average position of the photons, it also influences the standard deviation about this average. Isotropic scattering maximises the spreading of photons, but in an extreme case where for example at every nucleus 90% of the photons move in the same general direction,

they will stick together for a longer period and therefore the size of a "light cloud" will grow more slowly. This is an effect that shows up if we have a highly fluctuating density field on small scales, a case in point being the simulation of the filaments of large-scale cosmic structures.

We consider a density distribution that is homogeneous in the y- and z-direction but highly fluctuating in the x-direction. For the probabilities to travel into the dense or underdense regions, we again use Eq. (16) but with the difference that now d and u no longer denote global directions. We describe the transportation process by a binomial distribution. If there are no large scale-density contrasts, the drift is zero on average, but for the standard deviation we find

$$
\begin{aligned}
\sigma(N) &= \left\langle \sqrt{N\,p\,(1-p)} \right\rangle \\
&= \left\langle \sqrt{N\left(\frac{1}{2} + \frac{E(x)}{2}\right)\left(\frac{1}{2} - \frac{E(x)}{2}\right)} \right\rangle \\
&= \frac{\sqrt{N}}{2}\left\langle \sqrt{1 - E^2(x)} \right\rangle,
\end{aligned} \tag{21}
$$

where N is the number of sweeps. For small values of E, this reduces to

$$\sigma(N) \approx \frac{\sqrt{N}}{2}\left(1 - \frac{\xi^2}{32}\left\langle \left|n'(x)n(x)^{-4/3}\right|^2 \right\rangle\right). \tag{22}$$

This factor is always smaller than unity, indicating a reduction in the spreading of the photons. This effect can be significant for small-scale fluctuations with either a very high amplitude or a very short length. The effect slowly becomes smaller if the number of nuclei is increased. The value of $E(x)$ comes close to unity or exceeds unity only if the characteristic density fluctuation length is smaller than a Delaunay length, which we had pointedly excluded.

3.3. Effects on ballistic transport

For ballistic transport, problems similar to those of diffusive transport arise but that the transport is locally anisotropic complicates the picture. We first describe some properties of this kind of transport on a homogeneous grid to appreciate deviations from the "normal" case later on.

We identify two distinct phenomena that photons travelling ballistically may experience: deflection and decollimation. Deflection is here understood as "loss of direction", where the direction is given by the vector sum of the three most forward pointing directions. Decollimation is defined to be the effect of the increase in opening angle of a beam of photons as they are transported ballistically. The first phenomenon depends on the evolution of the vector sum of the three most forward directions, whereas the second phenomenon is related to the angular separation between these directions individually. In the case of a homogenous distribution of nuclei, the net effect of deflection will vanish because there is no preferential direction in the grid.

3.3.1. Decollimation

As stated in Sect. 2.5.2, the angular resolution, and therefore the minimal opening angle, is a property of the Voronoi cell and is thus fixed for the chosen triangulation. To exemplify this, we consider a typical Voronoi nucleus in 3D, connected to Λ

---

[9] It may surprise the reader that values for $E(\boldsymbol{x})$ and $\mathcal{D}$ are taken to be local, while the argument seems to involve a domain in which these values could change. What happens is that we adopt the *local* values for the *whole* domain in Eq. (18).
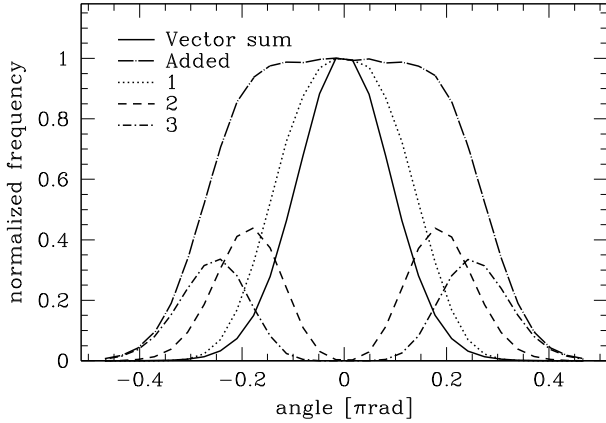
Fig. 7. Normalised distribution of angles between the incoming direction and the vector sum of the (three) most forward pointing edges (solid line) and the separate most forward edges (dotted, dashed and dot-dashed lines) for a homogeneous distribution of nuclei. The distribution of the most forward edges added is shown as the long dot-dashed line with label "Added" and is related to the decollimation effect. The standard deviation ($FWHM/\sqrt{\ln 256}$) is about 39° for the added edges and 15° for the vector sum of the edges.

Fig. 8. The projected step-size in the *x*-direction as a function of sweeps together with a least squares fit for the unweighted ballistic transport (solid line) and with ballistic weights as described in Sect. 4.2 (dashed line). A region indicating unit standard deviation is shaded in grey around the markers. Error bars correspond to $\sigma/\sqrt{N-1}$, where σ is the standard deviation and N the number of experiments executed. For the uncorrected case, the fitted value for the deflection angle θ_D in Eq. (24) is 39° ± 1%. For the weighted case, we find $\theta_D = 26° \pm 3\%$.

neighbouring nuclei. The expectation value for the solid angle, Ω, subtended by each edge is thus

$$\Omega = \frac{4\pi}{\Lambda} \approx \frac{\pi}{4}. \qquad (23)$$

In Fig. 7, the distribution of angles is given for a grid of 10^5 homogeneously placed nuclei in three dimensions. For the vector sum, the average departure from the incoming direction is about 15° (solid line). This implies that a photon loses all knowledge of its original direcion in typically $(90/15)^2 = 36$ steps.

For the distribution of the three separate most forward edges, we find a standard deviation of about 39°, which means that after $(90/39)^2 \approx 5$ steps the photon has lost all memory of its original direction. We note that the width of the vector sum of the weighted edges is smaller than that of the most forward directed edge (indicated by "1" in the figure) alone.

In general, the gradual loss of direction is not a major concern since most sources emit isotropically anyway, but the effect becomes important when many edges are traversed, because then the photons behave diffusively, producing an intensity profile that deviates from the correct $r^{-(d-1)}$-form. Simulations in which the mean free path for scattering or absorption is much smaller than 5 edges are fine in this respect, because then the ballistic photons never enter this random walk regime (see also the discussion in Sect. 7). To observe the implications of this statistical statement for the transport of photons, we construct a triangulation of a random point distribution containing 10^5 homogeneously placed nuclei in a cube of unit dimension. In the centre, we define a small spherical volume of radius 0.05 and place a number of photons in each nucleus contained in this volume. The photons are assigned a direction by sending them along the edge whose direction is maximally parallel to one of the coordinate axes (we select the positive *x*-axis). When applying our ballistic transport method, the photons therefore begin to move in the positive *x*-direction with a step-size equal (on average) to $\mathcal{D} \cos \theta_D$, where θ_D is the mean decollimation angle. Every step means a multiplication by a factor $\cos \theta_D$, until after infinitely many steps the effective step size in the *x*-direction is zero. In
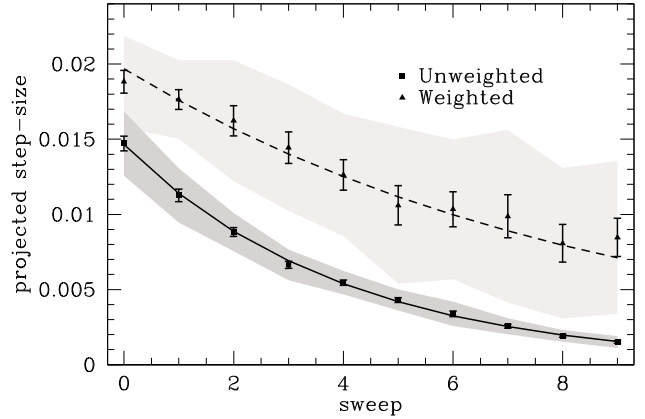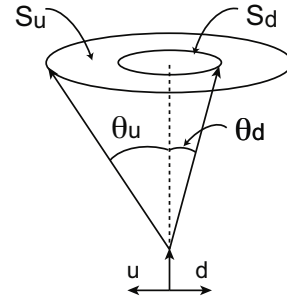

Fig. 9. Geometry of radiation travelling perpendicular to the gradient direction. The deflection angle toward the underdense region, θ_u, scales with the radius of the area S_u and similarly for the deflection angle towards the overdense region, θ_d.

Fig. 8, the step-size as a function of sweeps is shown together with a fitting function of the form

$$f(N_s) = A \cos(\theta_D)^{N_s}, \qquad (24)$$

where N_s is the number of sweeps. We find that without ballistic weights (filled squares; see Sect. 4.2 for the description of ballistic weights) $\theta_D = 0.67 \pm 1\%$ (39° ± 1%), in accordance with the value obtained from the grid statistics presented in Fig. 7.

3.3.2. Deflection

We are now ready to quantify the effect of the anisotropy of the triangulation on the ballistic transport of photons, which travel along the three edges closest (in angular sense) to the incoming direction. For the sake of simplicity, we estimate the deflection for radiation travelling along the most forward pointing edge and discuss the applicability to three edges afterwards.

We consider photons streaming perpendicular to the gradient direction (see Fig. 9 for the geometry of this situation.) The standard deviation in the deflection of the outgoing edge with respect to the incoming direction is typically 15° (see Fig. 7) for a homogeneous grid but in general depends on the local value for the gradient. Referring to Eq. (23), the expected opening angle depends on the effective number of outgoing edges in that

direction. In other words, as the anisotropy increases the number of edges pointing toward the overdense region, the angular resolution increases accordingly. This motivates one to define the direction-dependent number of outgoing edges, Λ_{eff}, to be

$$\Lambda_{\text{eff}}(\phi) = \Lambda[1 + E(x)\cos\phi], \tag{25}$$

where ϕ is the angle with the gradient direction. If we interpret the solid angle as a projected circular area on the unit sphere, we can estimate the maximal deflection angle, θ_{d}, for ballistic transport as

$$\theta_{\text{d}} = \arcsin\sqrt{\frac{4}{\Lambda_{\text{eff}}(\phi)}}. \tag{26}$$

For a homogeneous distribution of nuclei, this angle equals approximately 30° with a typical value of 15° being expected from the analysis shown in Fig. 7. If we include this empirical factor of one half in Eq. (26) and approximate the arcsine by its argument (correct to within 1% for angles smaller than $\pi/12$), we obtain

$$\theta_{\text{d}} = (\Lambda[1 + E(x)\cos\phi])^{-1/2}, \tag{27}$$

where we have used Eq. (25) to substitute for Λ_{eff}. This result can be approximated to first order by

$$\theta_{\text{d}} \simeq \Lambda^{-1/2}\left[1 - \frac{E(x)\cos\phi}{2}\right]. \tag{28}$$

To obtain the deflection per step over the grid, we average θ_{d} over azimuthal angle while projecting along the direction of the gradient

$$\theta_{\text{eff}} = \frac{1}{2\pi}\int_0^{2\pi}\theta_{\text{d}}\cos\phi\,\mathrm{d}\phi \tag{29}$$

$$= -\frac{E(x)}{4\sqrt{\Lambda}}. \tag{30}$$

The sign of θ_{eff} is negative, which means that the resulting deflection is into the region of lower density. This result might at first surprise the reader. One could naively predict the photons to deflect into the direction of higher density (similar to the diffuse drift) but the situation is exactly the reverse for ballistic deflection.

We note that this effective deflection angle is an upper limit to the deflection encountered in a simulation because of the following. The effect is maximal for radiation travelling perpendicular to the direction of the gradient and this is the situation we have used as a starting point for the above derivation of θ_{eff}. Secondly, that $\theta_{\text{d}} < \theta_{\text{u}}$ increases the likelihood of selecting edges in the overdense region effectively diminishing the deflection, an effect that we have neglected in the derivation above. To include this effect, one would have to know the distribution of outgoing edges as a function of angle with the gradient, and assign a probability to the selection of an edge accordingly. As we see in Sect. 5.3, the omission of this effect does not seem to be of much importance to our predictions.

Sending radiation along three edges rather than one decreases the effect of deflection. This is expected because the deflection of one edge is larger than that of the vector sum of three outgoing edges as we saw in the case of a homogeneous grid.

The growth of the deflection when traversing the grid can be found by dividing Eq. (30) by the typical step-size, $\mathcal{D}$

$$\frac{\Delta\theta_{\text{eff}}}{\Delta l} = \frac{1}{16\sqrt{\Lambda}}\frac{\nabla n(x)}{n(x)}. \tag{31}$$
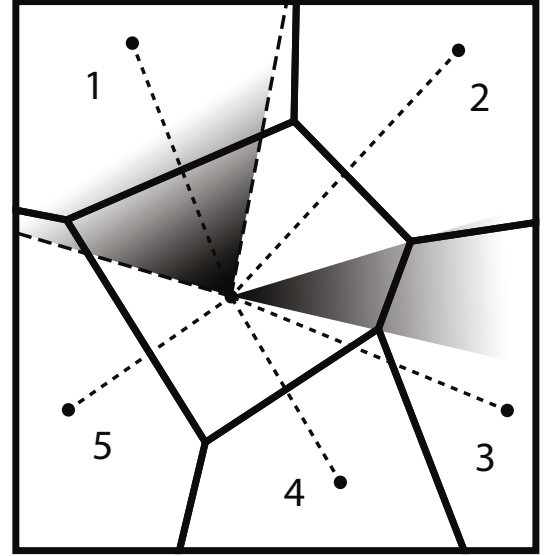
Fig. 10. Solid angles for two edges in the case of the Voronoi weighting scheme (cell 3) and the icosahedron weighting scheme (cell 1).

As for the drift length of Eq. (20), we can define a deflection length, L_{def}, at which the cumulative deflection is equal to say, $\pi/4$,

$$L_{\text{def}} = \frac{4\pi\sqrt{\Lambda}n(x)}{\nabla n(x)} \approx 50\frac{n(x)}{\nabla n(x)}. \tag{32}$$

Comparing with Eq. (20), we see that both the diffuse drift and the ballistic deflection place approximately the same restrictions on the box size, the only difference being a factor of 50 instead of 8. The interpretation again is simple. If $L_{\text{def}}(x)$ is strictly larger than say five times the box size, the deflection will be less than one-fifth of $\pi/4$ in travelling across the box in a "straight" line. We recall that this effect is added to the expected decollimation from Sect. 3.3.1.

4. Weighting schemes

We describe several possible ways to correct for the unphysical effects described in Sect. 3.

4.1. Diffuse transport

A straightforward cure of the problems addressed in Sects. 3.2.2 and 3.2.3 (diffuse drift and clustering, respectively) is to assign weights w_i to the edges emanating from a given nucleus in such a way that the anisotropy vanishes. This means that the fractions of the quantity transported to the neighbours are no longer equal to $1/N$ but directly proportional to the solid angle that the corresponding Voronoi face spans. We refer to Fig. 10 for an example in two dimensions, the three-dimensional case being analogous. We explore this possibility and implement three different weighting schemes in our method, each with their specific virtues and drawbacks:

1. Voronoi weights: based on the natural properties of the triangulation. Its advantages are that it is automatically and "naturally" adapted to the physics of the transport problem. Its disadvantage is the statistical noise inherent to the procedure.
2. icosahedron weights: based on a division of the unit sphere using the icosahedron. Its advantages are that it is flexible
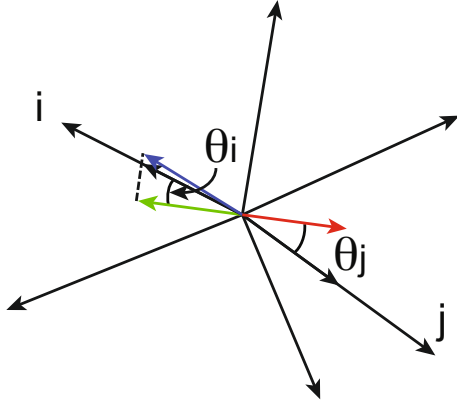
Fig. 11. Geometry of the COG weighting procedure.

(the procedure does not depend on type of triangulation) and that it is refinable. Its main disadvantage is that it is computationally expensive.

3. Distance weights: based on the distance to a neighbour squared. It main advantage is that is very fast. Unfortunately we have only empirical evidence of its correctness.

4.1.1. Centre of gravity weighting

In all three weighting methods, the sum of the weights equal unity, guaranteeing conservation of photons. In addition, the *vector* sum of the weighted Delaunay edges emanating from a nucleus should be zero to conserve momentum of the radiation field. We obtain this by adjusting the weights of the (two) edges most parallel and anti-parallel to the "centre of gravity", Ψ, of the nucleus defined by

$$\Psi = \sum_i w_i \hat{r}_i, \tag{33}$$

such that in that direction the magnitude of Ψ vanishes, $\hat{r}_i$ denotes the direction of the i-th Delaunay edge (see Fig. 11). The vector sum of all (weighted) Delaunay edges (black arrows) is non-zero (red arrow). The Delaunay edges j and i are most parallel and anti-parallel to this vector sum respectively. Their weights are adjusted such that the vector sum vanishes in its current direction. To this end, the vector sum and its reflected counterpart (green arrow) are projected on j and i, indicated with the smaller black arrows. Half of this projection is added to edge i and half is subtracted from j. The resulting vector is shown in blue and it exactly cancels the vector sum. The adjustment of weights can still result in a non-zero (although smaller) vector sum in some other direction. The above procedure is repeated iteratively until the norm of the vector sum is smaller than a predefined tolerance. In our experience, this procedure reaches a (relative) tolerance of 10^{-7} within twenty iterations for the Voronoi method and about ten for the icosahedron and distance weighting schemes.

4.1.2. Voronoi weighting

The Voronoi weighting scheme uses the faces of the Voronoi cells to calculate the w_i for each nucleus by estimating the solid angles subtended by the walls of the Voronoi regions, normalised to unity. The weights are then

$$w_i = \frac{S_i d_i^{-2}}{\sum_j S_j d_j^{-2}}, \tag{34}$$

where S_i denotes the surface of the Voronoi face perpendicular to the Delaunay edge connecting the current nucleus and its i-th neighbour, and d_i is the length of that edge (because the Voronoi face cuts the Delaunay edge in the middle, $0.5d_i$ being the distance from the nucleus to the face). We note that Eq. (34) is an approximate expression neglecting projection effects for large angles. With some computational effort, this estimate could be refined. The solid angle subtended by a Voronoi face depends on the size of the cell but also on the precise position of the nuclei. Referring to Fig. 10, we see that cell "3" has a relatively small surface because its nucleus is close to that of neighbour "4" *and* its nucleus is a bit further from the central nucleus than that of neighbour "4". If that last statement were reversed, neighbour "4" would have the smaller surface and would thus get the smaller weight. This property may seem harmful at first but it is of stochastic nature, meaning that some noise will be introduced but no systematic error.

To demonstrate our method, we construct a Delaunay triangulation of 10^5 nuclei in three-space with a linear gradient in $n(\mathbf{x})$ along the horizontal direction which runs from 0.005 on the left to 0.995 on the right. As a measure of the anisotropy in orientations of Delaunay edges, we take the angle between an edge and the direction of the gradient and plot the number of edges in an angular bin (see Fig. 12). Because we are interested in the relative deviation from a horizontal line (which would correspond to the isotropic situation), the results are given as a fraction of the average, $f(\theta)$. The data displayed in the topmost panel corresponds to the weighting schemes described above, which can be thought of as a basic correction plus a refinement thereof (the "centre of gravity" correction). We show the effects on the angular distribution of the edges as we apply these corrections cumulatively.

The initial anisotropy apparent from the inclination of the line labeled "unweighted" is reduced significantly (to about half its original value) after applying the Voronoi weighting alone (dashed line). After application of the "centre of gravity" correction, the scatter around the isotropic value of unity is below 0.25%, except at the outer edges where the normalisation dramatically increases the errors.

Apart from the anisotropy caused by the gradient, the triangulation shows some noise of order 0.5% itself (the light grey areas around the uncorrected lines in the three panels having a width of one standard deviation). After all weighting has been applied, some noise remains (a unit-standard deviation area is shaded in dark grey). This noise is related to features of the triangulation itself. If the triangulation itself has more edges in a certain direction, this cannot be corrected with a *local* weighting scheme because it is a *global* property subject to chance. This noise can be reduced by either placing more points, or, equivalently, constructing several instances of the same triangulation and averaging over the results.

Because all the information needed for the Voronoi weighting scheme is intrinsic to the tessellation and its triangulation, the associated computational overhead is potentially small. Unfortunately, in most tessellation software, the areas of the Voronoi walls are not computed with the other properties of the tessellation. Calculating these areas is computationally costly because in three dimensions the walls are generally irregular polygons with M vertices where $M \geq 3$.

4.1.3. icosahedron weighting

The second method is based on an "independent" division of the unit-sphere into M (approximately) equal parts. We take
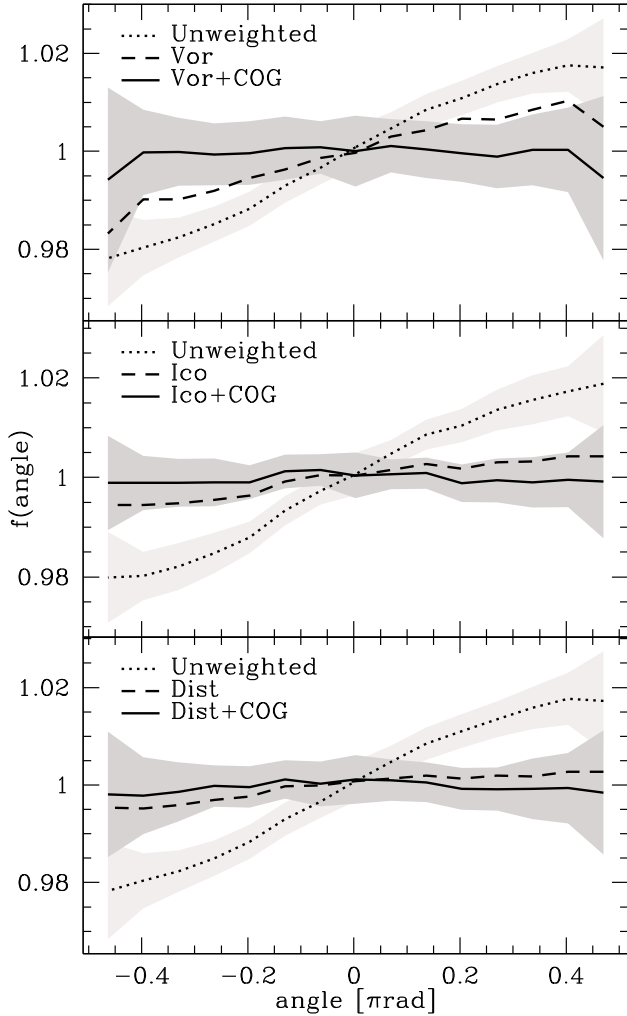
Fig. 12. Fraction of edges, $f(\theta)$, with angle $\pi - \theta$ with respect to the direction of the linear gradient as a function of θ for different cumulatively applied corrections with the Voronoi (*top panel*), icosahedron (*middle panel*) and distance weighting scheme (*bottom panel*). The results are averaged over 100 different realisations of the grid to suppress shot noise. Unit standard deviation regions around the "unweighted" curve and the final result are shaded in light and dark grey, respectively. As a result of the anisotropy of the triangulation, more edges point towards the overdense region (to the right) in the uncorrected case. Note that due to normalization, the results at the extreme ends are subject to noise.

the M vectors (originating in the nucleus under consideration) that point to these parts and assign weights w_i to the outgoing Delaunay edges as follows. We take a vector and calculate the N dot products with the Delaunay edges. The Delaunay edge that has the smallest dot product has a fraction $1/M$ added to its weight. In the icosahedron scheme, the weight is thus proportional to the solid angle a Delaunay line occupies considering the angular vicinity of its neighbouring edges (in 2D the solid angle is thus bound by the two bisectors shown as dotted lines in Fig. 10).

We chose the icosahedron as the basis of our weighting scheme. We use vectors to the middle of its 30 edges and its 12 vertices, yielding 42 reference vectors.

One significant advantage of the icosahedron method is that it is independent of the nature of the triangulation and is therefore very flexible. It becomes more accurate as the division of space is refined (M is increased) by taking other tessellations

of the unit-sphere. The computational cost, however, scales linearly with M forcing us to trade off accuracy with speed. Unfortunately this "independence" also has a drawback: the reference vectors are oriented statically in space, introducing a systematic bias in those directions. To reduce this effect, one is forced to add some random noise to the procedure, for example by applying random rotations of the whole icosahedron, another computationally costly operation.

After the correction with icosahedron weights (see middle panel of Fig. 12, dashed line), the anisotropy decreases below the 0.5% level. This immediately shows the strength of this method over the more noisy Voronoi scheme (compare also the unit standard deviation regions in dark grey).

4.1.4. Distance weighting

Empirically we found that in 3D the square of the distance between nuclei is also a robust estimator of w_i. This quantity is readily calculated and provides by far the most rapid solution to the problem at hand. After the initial correction (see bottom panel of Fig. 12, dashed line), the anisotropy of edges diminishes to values lower than 0.5% even slightly better than in the icosahedron scheme. The deviations from the ideal isotropic case after the COG correction are of the same order as in the Voronoi and the icosahedron case.

We could not find a valid explanation for the success of this method. Intuitively, one would think that the opening angle, Ω, of a Voronoi wall with respect to its nucleus would scale as r^{-2} rather than r^2. To find a mathematical reason for the proportionality between Ω and r^2, one would have to delve more deeply into the field of computational geometry which is beyond the scope of this text.

4.2. Ballistic weighting

Assigning weights to the outgoing edges as described above removes the drift and clustering problems for diffusive transport described in Sect. 3.

The effects of anisotropy in the ballistic case are intrinsically more challenging to correct because it is not a priori clear how the anisotropy of all outgoing edges of a nucleus should be used to choose three weights for the outgoing edges. As described in Sects. 3.3.1 and 3.3.2, in the ballistic case we must distinguish between decollimation and deflection first one of which the dominates the overall "loss of direction". To diminish the decollimation of a beam, we can assign weights to the most forward pointing edges. If we make these weights somehow proportional to the inner product of the edge and the incoming direction, the most forward pointing edges transport most of the photons.

There are many possible ways to assign weights to the D most forward directed edges, which each optimise different aspects of the transportation process. If the exact direction is important, for instance, the weights should be chosen such that the vector sum of the resulting edges points straight ahead. On the other hand, minimising the decollimation will in general yield a different set of weights, those that maximise the length of the vector sum.

From this myriad of possibilities, we choose a very simple and computationally cheap approach. To edge j we assign the weight w_j given by

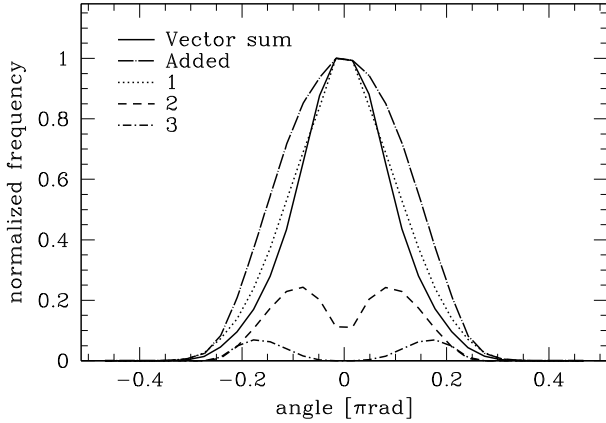$$w_j = \frac{\cos(\theta_j)/\sin(\theta_j)}{\sum_j \cos(\theta_j)/\sin(\theta_j)},\tag{35}$$

Fig. 13. Normalised distribution of angles between the incoming direction and the vector sum of the (three) most forward pointing edges (solid line) and the separate most forward edges (dotted, dashed and dot-dashed lines) for a homogeneous distribution of nuclei with ballistic weights. The distribution of the most forward edges added is shown as the long dot-dashed line and labeled "Added". The standard deviation ($FWHM/\sqrt{\ln 256}$) is about $26°$ for the added edges and $16°$ for the vector sum of the edges. Note that the width of the distribution of the single most forward pointing edge poses a definite lower limit to the width of the "Added" lines.

where θ_j is the angle between the incoming direction and edge j. The division by the sine of the angle places extra emphasis on the edges with the smallest inner product.

Applying this weighting scheme to the point distribution used to produce Fig. 7 yields the distribution of edges shown in Fig. 13. As specified by Eq. (35), the ballistic weights have the desired effect of decreasing the width of the distributions of the edges used in ballistic transport.

In Fig. 8, evolution of the step-size of ballistic transport in the weighted case is shown with crosses. The decollimation angle per step is substantially smaller than in the case without weighting ($26°$ compared to $39°$). This decrease in decollimation angle consequently relaxes the requirement that the number of ballistic steps must remain below 5. Including ballistic weights typically allows for up to 12 ballistic steps before the original direction is lost.

Finally, there are cases where the anisotropy of edges emanating from a cell cannot be solved by any weighting scheme. If there is no edge in a given direction, the radiation cannot go there, regardless of the weight values. One should begin with a reasonably isotropic triangulation to apply a weighting scheme in a useful way. In the case of Delaunay triangulations in three-space, this is almost always the case.

4.3. DCT throughout the grid

A conceptually different solution to the problems described in Sect. 3 is to apply the direction-conserving transport from Sect. 2.5.3 throughout the simulation domain. As the angular direction of the radiation is effectively decoupled from the grid in this approach, all drift, clustering, decollimation, and deflection are solved for at once. The cone containing the nuclei that receive radiation will however still be dependent on the grid itself as already pointed out in Sect. 2.5.3.

5. Numerical examples

After considering the various systematic effects affecting the *SimpleX* algorithm, we now present some sample cases that demonstrate them. In general, all of the effects described above occur simultaneously, but for transparency we analyse them in isolation.

5.1. Effects on diffusive transport: drift

We now proceed by describing the numerical experiment designed to show the effects of diffuse drift. The simulation domain of unity volume in three dimensions is filled with 5×10^5 nuclei subject to a gradient in the point density of the form $n(x) = x$. We choose this linear form because it locally approximates every other type of gradient. The number of nuclei results in roughly 32 steps across the box along the gradient direction and 38 in the directions perpendicular to the gradient. These numbers allow for most of the photons to travel through the box for more than 100 steps before being captured in the absorbing boundaries.

At the site closest to the centre of the domain, a number of photons is placed. Neither the outcome nor the speed of our simulation depends on this number as we use floating point numbers to represent photons.

Photons are transported over this grid using diffusive transport without absorption. With every sweep, the photon cloud is expected to grow in size. In the case of a homogeneous point density, the photons will be distributed normally, as must be expected for pure diffusion. The gradient in the point density will distort the form of the distribution function for two reasons. First, the mean free path on the grid, $\mathcal{D}$, scales with the point density according to Eq. (9) allowing photons to diffuse faster into the underdense regions where the step sizes are larger. Second, the drift phenomenon described in Sect. 3.2.2 will counteract this physical diffusion and move the cloud into the overdense region.

To separate these two effects, we performed a one-dimensional Monte Carlo simulation of 2×10^6 "random walkers" that take steps with a size given by the recipe of Eq. (9). The experiment described above is emulated in one dimension but without the Delaunay grid as an underlying structure. The random walkers are thus expected to experience the *physical* diffusion into the underdense region only. The unphysical drift is caused exclusively by the Delaunay grid and will not be present in our results.

In Fig. 14, the intensity-weighted position of the photon cloud (along the direction of the gradient) versus the number of sweeps in the simulation is shown for *SimpleX* and the Monte Carlo experiments in the cases of both with and without weights[10]. We can see that the behaviour conforms to our expectation. The weighting corrected *SimpleX* result coincides with the Monte Carlo as shown in the bottom panel.

Furthermore, we took our drift description Eq. (13) and applied it to the Monte Carlo experiment thus introducing a drift toward the overdense region similar to that experienced by a photon in *SimpleX*. The effect counteracts the physical diffusion into the underdense region resulting in a positive slope for the position of the photon cloud as a function of sweeps (see top panel of Fig. 14.) This procedure thus provides a direct quantitative check of the correctness of Eq. (13).

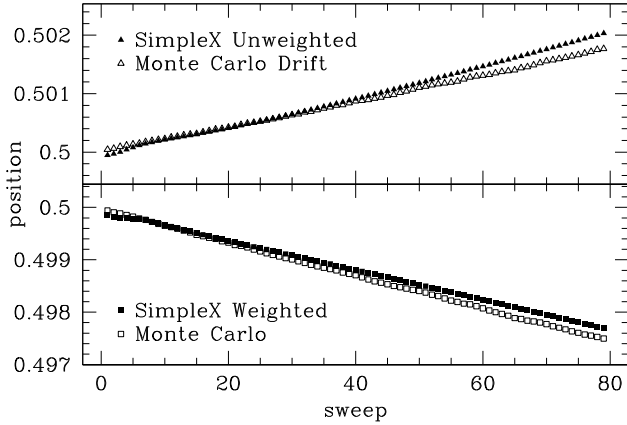[10] We used icosahedron weights in this case but this choice does not influence the results.

Fig. 14. Intensity-weighted position of a photon cloud released in the centre of a simulation domain with a linear gradient in the number denisty of nuclei as a function of the number of sweeps. Results obtained with *SimpleX* are shown with filled symbols and results obtained by the Monte Carlo experiments are indicated with open symbols. We use triangles and squares in the corrected and uncorrected case, respectively.

Fig. 15. Normalised standard deviation of the intensity-weighted positions of a photon cloud expanding in a distribution of nuclei with small-scale gradients with and without weights (thick and thin solid lines, respectively) and the analytical expectations according to Eq. (21) (dashed line). A dotted line at $\sigma/\sigma_{\text{hom}} = 1$ is included to guide the eye.

The slopes of the Monte Carlo experiment agree to within a thousandth of a degree with the *SimpleX* results for both the uncorrected and weighted results. This implies that the weighting schemes discussed in Sect. 4 do not only correct the orientation of the edges in a statistical sense (as shown in Fig. 12) but also allow for correct transport over these edges. This may seem a trivial statement, but despite everything being fine in a global sense, local anomalies may prevail. The transport of photons, however, depends strongly on the local correctness of the weighting scheme and is thus a more stringent test. Furthermore, the recovery of the *SimpleX* results with the Monte Carlo experiments suggests that Eq. (13) describes the drift phenomenon accurately in a quantitative sense.

5.2. Effects on diffuse transport: clustering

As seen in Sect. 3.2.3 the expansion of a photon cloud is stalled by small (relative to the simulation domain) scale gradients in the grid. To illustrate this effect performed the following experiment. The simulation domain is again given by the unit cube with a large number of photons at the centre. The 5×10^5 nuclei are distributed according to the probability distribution

$$n(\boldsymbol{x}) = 0.2 + 0.8 \sin^2(\omega|\boldsymbol{x}|), \tag{36}$$

where $\omega = 20$. The density of nuclei thus inhibits concentric variations with a amplitude of 0.8 on a homogeneous background of 0.2.

We now prepare a similar simulation with a homogeneous distribution of nuclei where the box-size measured in units of $\mathcal{D}$ is the same. A comparison of the spread of the photon cloud in the homogenous setup with that given by Eq. (36) provides a direct measure of the effect described by Eq. (22).

Application of a weighting scheme for diffusive transport described in Sect. 4 should remove the difference between the spread of the cloud in the two cases described above. As a check, we also compare the results to the analytical result given by Eq. (21) and the expected spread of the photon cloud in the homogenous case (which is simply $\mathcal{D}\sqrt{N}/2$).

In Fig. 15, the spread of the photon cloud in terms of the normalised standard deviation in the intensity-weighted positions is
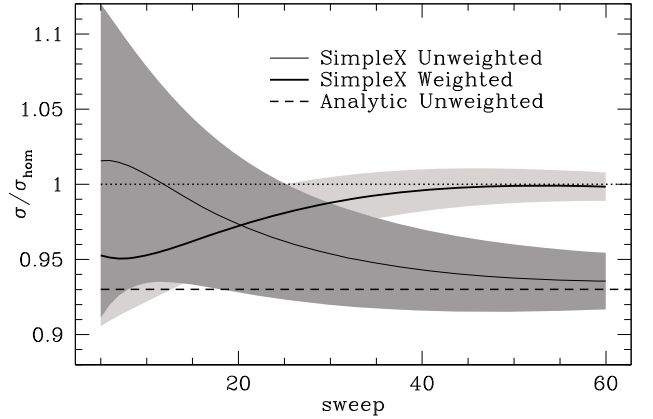
shown for the inhomogeneous point density given by Eq. (36) (solid lines) and the analytical prediction (dashed line). The data are obtained from twenty runs with different realisations of the grid.

As expected, the photon cloud expands (almost 6%) more slowly when no weights are used in the case of small-scale gradients (thin solid line). Application of the weighting scheme results in a cloud that (after a slow start) conforms to the expected size (dotted line at $\sigma/\sigma_{\text{hom}} = 1$). The analytical model predicts this behaviour to within 3% after 30 sweeps, and increasingly poorly for fewer sweeps (although the deviation remains below 10%). The larger deviations for fewer sweeps are caused by the cloud size (expressed in standard deviations) being small and the results are divided by this small number. We note that the unit standard deviation region for the weighted case is narrower in the weighted case (light gray) than the unweighted case (dark gray). This is expected because the weighting scheme corrects for local anisotropies and thus reduces the noise in the diffusive transport.

In the homogeneous case we have verified that applying a weighting scheme does not alter the expansion speed of a photon cloud significantly, as expected. We can thus conclude that, although clustering can impose a substantial effect on the expansion of diffuse radiation, our weighting scheme corrects for it appropriately.

5.3. Effects on ballistic transport: deflection

To study whether anisotropy has any effect on the direction of a beam of photons, we considered a triangulation of a random point distribution containing 5×10^5 nuclei placed in a cube of unit dimensions with a linear gradient along the x-direction. In the centre, we included a spherical volume of radius 0.05 and place a number of photons in each nucleus contained in this volume. The photons were assigned a direction by sending them along the edge whose direction is maximally perpendicular to the x-axis. The simulation was executed with ballistic transport using both one and three outgoing edges and in addition with the direction-conserving implementation of *SimpleX* (as described in Sect. 2.5.3). Every run was repeated 10 times with different instances of the grid to suppress shot noise and obtain error estimates.
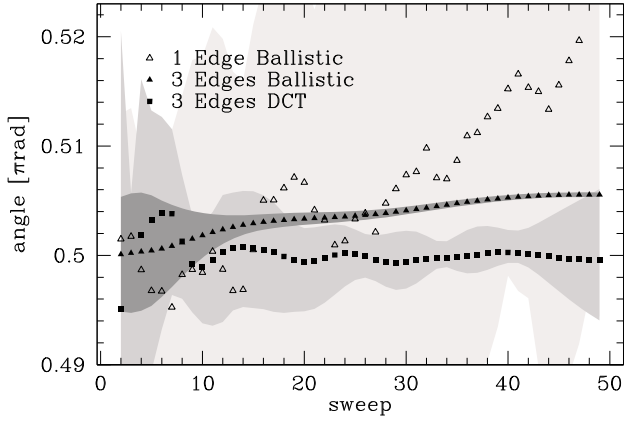
Fig. 16. Mean angular directionality of a photon cloud as a function of the number of sweeps. In this simulation, a linear gradient in the density of nuclei is present and the angle is measured relative to the direction of the gradient, so smaller values of the angle point toward the denser region. As expected, the direction-conserving implementation of *SimpleX* (as described in Sect. 2.5.3, indicated by filled squares) has no long-term loss of directionality, although it shows some oscillatory behaviour that dampens with time. Ballistic transport with one edge (open triangles) shows a deflection towards larger angles for number of sweeps of order $5 \times 10^{-4} \pi$ rad/sweep in accordance with predictions. Using three outgoing edges (filled triangles) diminishes the effective deflection by a factor of five. Unit standard deviation regions are shaded in grey for the three simulations.

When applying our ballistic transport method, the photons undergo small angular deflections into the underdense region as predicted in Sect. 3.3.2. Using Eq. (30), the expected effective deflection for this setup is $\theta_{\mathrm{eff}} = 5 \times 10^{-4}\pi$ rad/sweep, which yields a cumulative result of approximately 0.025π rad after 50 sweeps. This estimate is consistent with the result of the simulation with one forward edge denoted by the open triangles in Fig. 16. As expected, sending radiation along three edges decreases the deflection and fluctuation of the angular direction in general because radiation is distributed over many (3^{N_s}) edges, which quickly reduces shot noise with time. When using the direction-conserving implementation of *SimpleX* (filled squares), the radiation does not suffer from ballistic deflection.

6. Application

We illustrate how to apply the results of the above analysis to a more astro-physically relevant problem. We ask ourselves whether given a density (or opacity) distribution, how we can construct a Voronoi-Delaunay structure that keeps the described problems acceptably small while representing the physical problem as accurately as possible. This often means maximising the dynamic range with the prerequisite that low density regions have sufficiently high resolution.

6.1. Sampling function

The trade-off is thus between maximising dynamic range and minimising the strong gradients this inevitably introduces. In other words, we must investigate the effects that different sampling functions have on the triangulation and its transport properties. These functions translate the physical medium (expressed as an opacity or density map) to a point distribution $n(x)$ whose points form the nuclei of the triangulation. As mentioned in Sect. 3.2.2, the average Delaunay edge length can be associated

with the mean free path of the photons in a very natural way. This is achieved when $n(x)$ scales with the opacity (or density) to the D-th power (Ritzerveld & Icke 2006, Eq. (14))

$$n(x) = \Phi * \rho^D(x), \tag{37}$$

where Φ denotes a homogeneous Poisson process, D is the dimension of the propagation space, and $*$ denotes the convolution.

One drawback of using Eq. (37) is that the resulting point process, given a substantial density contrast, places many nuclei in dense regions and very few in underdense regions. For many applications, simulating the true mean free path may thus require a number of nuclei that is prohibitively high.

We therefore adopt a more flexible sampling function that behaves differently for the extremal densities of the grid. According to this function, the number density of nuclei that generate the Voronoi grid is given by

$$n(x) = 2\Phi * \left(y^{-\alpha} + y^{-D}\right)^{-1}, \tag{38}$$

where $y \equiv \rho/\rho_0$ and ρ_0 is a reference density that marks the transition between the two regimes of sampling power. In our applications, α will always be smaller than D (and even smaller than unity) to prohibit the over-emphasis on high density regions.

According to Eq. (20) and (32), the quantity that links the properties of the grid (density of nuclei and gradients therein) to the systematic effects described in the previous sections is $Q_n \equiv n/\nabla n$. We are now in the position to define, in a way analogous to Q_n, the quantity $Q_y \equiv y/\nabla y$, which can be measured over the physical density (opacity) field. As the sampling function of Eq. (38) translates the physical field to the density of nuclei, the measured value of Q_y and the upper limit of Q_n (posed by the maximally acceptable value for either L_{drift} or L_{def}) constrain the sampling parameters α and ρ_0.

6.2. Cosmological density field

We now apply this idea to a more realistic example and see what this all means in practice. A typical application wherein the strength of the *SimpleX* algorithm can be fully deployed is the epoch of reionisation (see Paardekooper et al. (2010) for an account of relevant test cases). Both the wide range of densities (four to five orders of magnitude) and the large number of sources (hundreds to thousands in realistic cosmological volumes) can be treated naturally by *SimpleX* due to the adaptive nature of the Delaunay grid and because the computational effort does not increase with increasing number of sources.

We now consider a typical (0.5/h Mpc comoving) cosmological volume (as used in test 4 of Iliev et al. (2006)) and construct a representative point set using constraints from analysis of the original data. In this specific case, the cosmological density field was presented as a regular grid of 128^3 equal size cells.

6.3. Constraints

Given the regular grid, the quantity Q_y can be determined for every pair of adjacent cells. The mean value of Q_y obtained is thus 1.6.

This value implies that if we would use a linear translation between the mass density of the original data and the number density of the nuclei of the Delaunay grid, the equality length (see Eq. (20)) would become $8 \times 1.6 \simeq 13$ and the deflection length of Eq. (32) becomes $50 \times 1.6 \simeq 81$. This means that radiation can travel 13 box-lengths before diffuse drift starts to
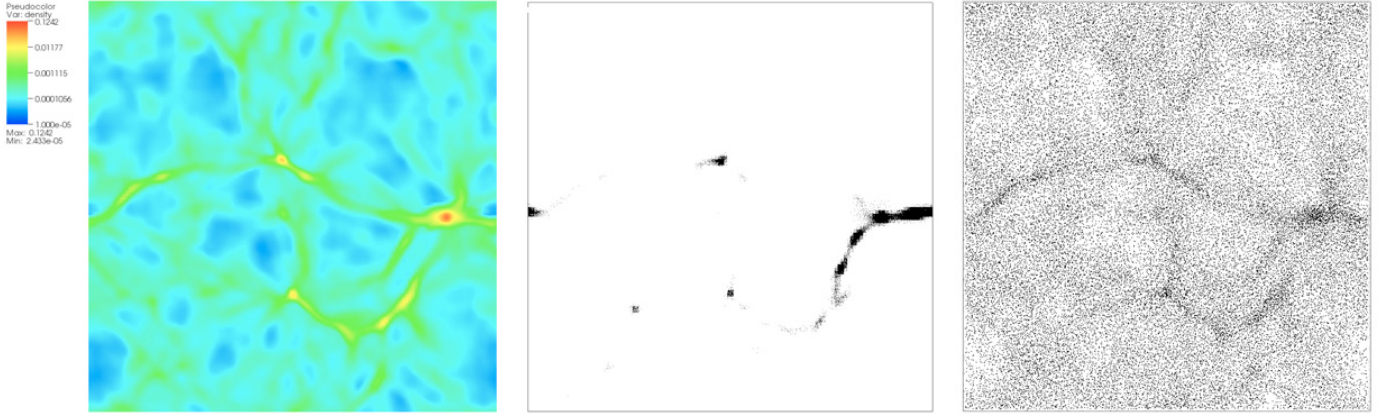
Fig. 17. Cut through a cosmological density field (*left panel*; colours indicate number density in logarithmic scale) sampled with 10^5 points using the sampling function of Eq. (37) (*middle panel*) and Eq. (38) (*right panel*) with the parameters obtained from analysis of the underlying density field.

dominate the transport of radiation, and 81 box-lengths before ballistic deflection reaches a cumulative magnitude of $\pi/4$.

This linear sampling could be performed using $\alpha = 1$ in Eq. (14) or, equivalently, $\alpha = 1$ and $\lim_{\rho_0 \to 0}$ in Eq. (38). Linear sampling is hardly ever desirable in a cosmological setting, however, as it tends to place the bulk of the nuclei in high density regions resulting in oversampling (many nuclei per grid cell of the original grid) of filaments and clumps and undersampling of voids.

We proceed by finding optimal values of our sample parameters, given the measured value of Q_y and a chosen value for the maximum allowed equality length. An upper limit to the equality length, by means of Eq. (20), immediately implies a maximal Q_n.

For example, if we set $L_{\text{drift}} = 40$ (and consequently $L_{\text{def}} = 250$), we see that we need to choose α and ρ_0 such that $Q_n = 5$. From Eq. (38), we can derive an expression that links the measured value of Q_y to Q_n and thus to the sample parameters, given by

$$Q_n = Q_y \frac{y^{-\alpha} + y^{-D}}{y \left(\alpha y^{-\alpha-1} + D y^{-D-1} \right)} \cdot \quad (39)$$

Solutions for $Q_n = Q_y$ exist only for certain pairs of α and ρ_0 as can be seen from the limit of Eq. (39),

$$Q_n^{\text{lim}} = \lim_{y \to \infty} Q_n = \frac{Q_y}{\alpha} \cdot \quad (40)$$

If we were to choose α at its maximal value of Q_y/Q_n^{lim}, we would therefore effectively insist that $\rho_0 \to 0$, resulting in the limit where all density regimes are sampled with the same power, α. Choosing α to be smaller but close to its extremal value maximises the dynamic range in the high density regions and allows ρ_0 to attain values where a substantial volume of the density field (namely the voids) is sampled with the advantageous power D.

Solving Eq. (40) for $Q_y = 1.6$, we find $\alpha = 0.32$ to be the maximal value. Taking the somewhat smaller value of 0.3, the corresponding value for ρ_0 is 3.7×10^{-5} cm^{-3} which is significantly higher than the lowest densities in the cosmological field, which are about 2.4×10^{-5}.

6.4. The grid

In the right panel of Fig. 17, a cut at $z = 0.5$ through the sampling defined by these parameters is shown. The middle panel shows

the point distribution one obtains when sampling with $\alpha = 3$ throughout the grid. This distribution does not accurately reproduce the low-density regions, placing almost all points in the dense filaments and their intersections. In contrast, the "hybrid" sampling method provides sufficient resolution in both the low- and high-density regions. For the $\alpha = 3$ sampling, the cell size in the filaments and dense clumps is many times smaller than that of the original regular grid. No information is carried, however, by this extra resolution, effectively wasting computational resources. As an extra constraint (apart from L_{drift} and L_{def}), one could demand that the smallest Voronoi volume is equal to the resolution of the original data. This could either be the highest AMR resolution or, in the case of SPH, the minimal smoothing length.

6.5. Speed considerations

Although we do not consider details here, the speed of *SimpleX* also depends on the form of the grid. Because in every sweep all nuclei are visited exactly once, the execution time of the method scales linearly with the number of nuclei. In turn, the number of sweeps needed to reach convergence roughly scales as the number of sweeps it takes to enable every point within the simulation domain to "communicate" its physical properties by every other location by an exchange of photons.

Now consider the point distribution in the middle panel of Fig. 17. The resulting grid will have many short edges in the high density clump in the east of the domain. For diffusive transport or ballistic transport over many (more than roughly 5) edges, such a clump will trap photons for many sweeps because their travelled distance after N sweeps is given by $\sqrt{N} \mathcal{D}$ where $\mathcal{D}$ is small. This is another reason not to use high sampling powers throughout the simulation domain.

7. Discussion

After identifying and correcting the various effects caused by anisotropy in the Delaunay grid, we discuss their implications in a broader context.

7.1. Prevention versus correction

It is impossible in general to define the perfect grid. As already pointed out, a large dynamic range inevitably leads to gradients

that, in turn, produce the unphysical effects described in this text. Although we have shown that these effects can be corrected by weighting schemes, these corrections are not fail-safe if the gradients are too strong. In particular, when the density of nuclei changes appreciatively on length scales smaller than $\mathcal{D}$ (or, more precise, $Q_n \leq 1$), the lack of edges towards the underdense region may lead to extreme decollimation as there are simply hardly any edges that point that way. In this case, a weighting scheme is not feasible as there are no edges to assign weights to in the underdense direction. We therefore need to begin with a fairly well behaved grid in the first place.

One could argue that if the grid is constructed such that the unphysical effects are below a predefined tolerance, the deployment of weighting schemes can be circumvented. On the other hand, this rather tight constraints on the grid and it might be preferable to retain a greater dynamic range (and thus structure) in the grid at the expense of the need for weighting.

An intermediate solution will often be the most viable option, where we retain the dynamic range of the data as much as possible while weighting schemes and DCT are employed at *certain locations* in the simulation domain only.

7.2. Number of steps versus L_{drift} and L_{def}

In Sect. 3, we determined the typical length scales on which the unphysical effects become important in a relative sense. Being cautious, we defined these length scales to many times the size of the simulation domain, although this is not necessary in most real-life situations because radiation typically travels only moderate distances along the grid. It might therefore be more intuitive to think about the number of steps a photon travels along the grid before being scattered or absorbed instead of L_{drift} and L_{def}. In the event of either absorption or scattering, the past of the photon is essentially erased and it starts a new life, so decollimation, deflection, and drift are basically "reset" to zero.

We can thus assess the possible harm of anisotropy in a simulation by monitoring the fraction of Delaunay length and physical mean free path, R, defined as

$$R \equiv \frac{\mathcal{D}}{l_{\mathrm{mfp}}} \cdot \tag{41}$$

First of all, R should not be much smaller than 1, because this would cause decollimation and in extreme cases even the simulation of straight light rays by a random walk (see also the discussion in Sect. 3.3.1).

In the limit of large R, however, a large portion of the photons will be absorbed after travelling along this edge. This is merely a resolution issue: the photons will never travel further than one Voronoi region away from the place where they ought to have been absorbed.

Using a sampling function of the form of Eq. (37) would result in R being a constant along the grid. If we use a more general sampling method, R is no longer a global constant. We can however still adjust the local optical depth for absorption with the local value of R. If we do so, the place where a photon finally becomes absorbed or leaves the simulation domain still has the right probability distribution, but the interpretation of intermediate photon densities in the simulation becomes less intuitive. The photon densities are not "time" densities but "step" densities, but now photons in regions with different densities will travel a different amount of mean free paths per sweep. If we are interested in the effect of the photons on the medium and in the directions of photons that leave the box, we are justified in sampling using

any other power than 3, as long as we make local corrections to the optical depth that are proportional to R.

7.3. A dynamic grid

We have argued that the ratio of the local mean free path to the Delaunay edges should be chosen with care to ensure meaningful results. Because the local mean free path can change due to changes in the medium properties, the Delaunay edge length should adapt accordingly to keep R fixed.

The *SimpleX* code has been extended to handle dynamic media (Paardekooper et al. 2010), where nuclei can be added or deleted during the simulation. This allows the triangulation to adjust itself to the (changing) local properties of the medium.

We can set up strict conditions under which a nucleus is deleted (and its attributes divided between its neighbours). A possible condition could be to delete a nucleus whenever the local mean free path of the ionising photons exceeds the average length of its outgoing edges. In this way, we would keep deflection and decollimation acceptably small in the case of ballistic transport.

8. Future work

In this section we discuss several limitations of the current *SimpleX* method and indicate a possible route forward to overcome these limitation in future versions of the code.

8.1. Multiple frequencies

In the current incarnation of *SimpleX*, a grey approximation is used where the effect of a source spectrum is taken into account by the use of effective, intensity-weighted, cross-sections. Implementation of a full multi-frequency treatment is not trivial because it formally requires a separate grid for every new frequency bin. In practice, however, we have found that by transporting similar frequencies over the same grid, the computational demands will not become prohibitive. A version of *SimpleX* incorporating multiple frequencies is currently under development and we postpone a discussion of related issues to future articles.

8.2. Cosmological redshift

For cosmological simulations, the expansion of space will shift the frequency of the transported photons. In our one-frequency approach, this is nothing more than a gradual loss of ionizing energy for the photons. In future multi-frequency versions of the code, more care should be taken with this issue especially when line-transfer is included.

In principle, relativistic "beaming" could also play a non-negligible role in simulations of large cosmological volumes. Owing to expansion of the universe, an absorbing parcel of gas will have different relative velocities to sources at different distances. The resulting enhancement of the observed intensity (Eq. (4.9) in Rybicki & Lightman 1986) can be substantial. This beaming could in principle be modeled in *SimpleX* by adjusting the weighting factors for diffuse and ballistic transport appropriately, but we leave a detailed analysis to future work.

8.3. Strong scattering

Finally, in the case of strong scattering (if the cross-section for absorption is negligibly small compared to the cross-section for scattering) the *SimpleX* method only converges asymptotically to the correct answer. This is because transport occurs on a cell-to-cell basis and this can take a large number of sweeps to bring all scattering particles in the simulation domain into equilibrium. This problem is well known and has been overcome by classical radiative transfer methods by using so-called accelerated lambda iteration methods.

In the cosmological applications of *SimpleX*, strong scattering is not, however, a dominant process, and we do not pursue an implementation of accelerated Lambda iteration schemes in our method in the near future.

9. Summary

We now summarize the main insights and results from the above analysis.

1. The *SimpleX* algorithm is a relatively new and non-standard method, whose systematic effects should be thoroughly analyzed. This assessment has two important purposes: first, exploring the boundaries of its reliability and accuracy and, second, increasing its region of application by improvements.
2. The mathematically transparent nature of the *SimpleX* algorithm allows a rigorous and general assessment of its systematic effects to be performed. Although only some of the described effects (diffuse drift and ballistic decollimation) need to be considered in typical applications (see Paardekooper et al. 2010), we have investigated all four in detail for completeness.
3. The use of a random Delaunay triangulation in the radiative transfer method *SimpleX* introduces global errors when the point-density is inhomogeneous. We have identified and quantified four distinct effects: "drift" and "clustering" of photons in diffusive transport, and "decollimation" and "deflection" in ballistic transport.
4. We have shown that decollimation become troublesome only when the number of traversed edges becomes larger than roughly 5 steps. This implies that one either preclude this regime or, when this is undesirable or impossible, correct for the unphysical behaviour.
5. A weighting method for ballistic transport has been shown to decrease the effect of decollimation significantly by pushing the limit for correct transport from 5 to 12 steps.
6. We have shown how drift and clustering can be adequately corrected for by adopting a weighting scheme. Three weighting schemes for diffusive transport have been discussed and compared.
7. The use of a direction-conserving variant of the ballistic transport has been introduced as an alternative to the weighting procedure and to prevent loss of angular direction in optically thin regions. This approach also provides a means of correcting for deflection, drift, and clustering. The computational cost and need for additional randomisation of the solid angle directions ensures, however, that the employment of DCT is not generally favourable.
8. Finally, we have applied our analysis to an astrophysically relevant example. This elucidated the intimate relation between the construction of a computational grid and the possible need for weighting schemes.

References

Abbott, D. C., & Lucy, L. B. 1985, ApJ, 288, 679
Delone, B. N. 1934, Bull. Acad. Sci. USSR: Classe Sci. Mat, 793, 7
Du, Q., Faber, V., & Gunzburger, M. 1999, SIAM Rev., 41, 637
Edelsbrunner, H. 2006, Geometry and topology for mesh generation, 1st edn. (Cambridge University Press)
Icke, V., & van de Weygaert, R. 1987, A&A, 184, 16
Iliev, I. T., Ciardi, B., Alvarez, M. A., et al. 2006, MNRAS, 371, 1057
Lloyd, S. P. 1982, IEEE Transactions on information theory, IT-28, No 2, 129
Mellema, G., Iliev, I. T., Alvarez, M. A., et al. 2006, New Astron., 11, 374
Mihalas, D., & Weibel Mihalas, B. 1984, Foundations of radiation hydrodynamics (New York: Oxford University Press)
Okabe, A., Boots, B., Sugihara, K., Chiu, S. N., & Kendall, D. G. 2000, Spatial tessellations: concepts and applications of Voronoi diagrams, 2nd edn. (Wiley)
O'Rourke, J. 2001, Computational Geometry in C, 2nd edn. (Cambridge University Press)
Paardekooper, J.-P., Kruip, C. J. H., & Icke, V. 2010, A&A, 515, A79
Ritzerveld, J., & Icke, V. 2006, Phys. Rev. E, 74, 026704
Ritzerveld, N. G. H. 2007, PhD Thesis, Leiden Observatory, Leiden University
Rybicki, G. B., & Lightman, A. P. 1986, Radiative Processes in Astrophysics, ed. G. B. Rybicki, & A. P. Lightman
Schaap, W. E., & Van de Weygaert, R. 2000, A&A, 363, L29
Vedel Jensen, E. B. 1998, Local Stereology, 1st edn. (World Scientific)
Voronoi, G. 1908, J. Reine Angew. Math., 134, 198